Pressure dependence of the $^4T_2$ and $^4T_1$ absorption bands of ruby to 35 GPa

Steven J. Duclos,* Yogesh K. Vohra, and Arthur L. Ruoff
Department of Materials Science and Engineering, Cornell University, Ithaca, New York 14853
(Received 6 September 1989)

The pressure dependence of the $^4A_2 \rightarrow {}^4T_2$ and $^4A_2 \rightarrow {}^4T_1$ absorption bands of ruby have been studied to 35 GPa using a luminescence excitation technique developed for use at high pressure in the diamond anvil cell. The quasihydrostatic (Ar medium) pressure dependence of the zero phonon lines, the crystal-field splitting parameter (Δ), and the Racah parameters B and C are determined. A significantly smaller variation of Δ is found for nonhydrostatic stress conditions for a ruby powder compact, and the implications of this on the pressure calibrations, lifetime measurements, and excitation of the R lines at high pressure are discussed.

I. INTRODUCTION

The R_1 and R_2 luminescence lines of the electronic spectrum of Cr^{3+} in Al_2O_3 (ruby) have been used extensively for measurement of pressure in the diamond anvil cell (DAC).[1,2] Calibration of the R_1 energy versus pressure has been done to 180 GPa in a nonhydrostatic environment,[3,4] and to 80 GPa in a quasihydrostatic environment.[5] The energy difference between the R_1 $[^2E(\overline{E}) \rightarrow {}^4A_2]$ and the R_2 $[^2E(2\overline{A}) \rightarrow {}^4A_2]$ luminescence lines has been used to estimate the nonhydrostaticity of the stress environment at the ruby site.[6,7] Recently it has been observed that above ~200 GPa observation and calibration become exceedingly difficult[8,9] since the luminescence intensity continuously decreases when the blue lines of an Ar-ion laser are used to excite the R lines through the $^4A_2 \rightarrow {}^4T_2$ absorption band. Also, investigations of the R-line lifetime, τ, versus pressure[10,11] have shown a significant dependence of τ on pressure and the details of nonhydrostaticity.[11] In order to understand the pressure dependence of the interrelated properties of energy, intensity, and lifetime of the R lines, an understanding of the *entire* electronic spectrum of Cr^{3+} in ruby is necessary.

For the purposes of this paper the Hamiltonian of the $3d$ electrons of Cr^{3+} in ruby can be written:

$$\mathcal{H} = \mathcal{H}_0 + \mathcal{H}_{\text{cubic}} + \mathcal{H}_{\text{Coul}} + \mathcal{H}_{\text{trig}} + \mathcal{H}_{\text{SO}}. \quad (1)$$

The first term, $\mathcal{H}_0$, is that of the Cr^{3+} ion and results in the usual (degenerate) $3d$-electron orbitals. $\mathcal{H}_{\text{cubic}}$ is the cubic (O_h) symmetry part of the crystal field originating from the O^{2-} ligands. It splits the one-electron $3d$ orbitals into two, e and t_2, separated by Δ, the crystal-field-splitting parameter, of order[12] 17 000 cm^{-1}. $\mathcal{H}_{\text{Coul}}$ represents the Coulomb interaction between the three $3d$ electrons of the Cr^{3+} ion, and is treated as a perturbation of the single-electron orbitals. This causes splittings of the e and t_2 orbitals of the order of the Racah parameters B (~ 500 cm^{-1}) and C (~ 3400 cm^{-1}), which are related to Slater integrals between the multielectron orbitals. The Cr^{3+} ion site is distorted from cubic to trigonal (C_{3v}) symmetry and $\mathcal{H}_{\text{trig}}$ is the trigonal part of the crystal field. It causes splittings of the Cr^{3+} levels of the order[13]

$$k \equiv -3\langle t_2 \mid \mathcal{H}_{\text{trig}} \mid t_2\rangle \simeq 800 \text{ cm}^{-1}$$

and (2)

$$k' \equiv \langle t_2 \mid \mathcal{H}_{\text{trig}} \mid e\rangle \simeq 400 \text{ cm}^{-1}.$$

The last term, $\mathcal{H}_{\text{SO}}$, is the spin-orbit interaction between the d electron and the Cr^{3+} nucleus which causes splittings characterized by[14]

$$\zeta \equiv -2\langle t_2 \mid \mathcal{H}_{\text{SO}} \mid t_2\rangle = 140 \text{ cm}^{-1}$$

and (3)

$$\zeta' \equiv -\sqrt{2}\langle t_2 \mid \mathcal{H}_{\text{SO}} \mid e\rangle \simeq \zeta.$$

$\mathcal{H}_{\text{trig}}$ and $\mathcal{H}_{\text{SO}}$ generally cause small splittings in the levels, but play a crucial role in mixing states and allowing transitions that would otherwise be spin or parity forbidden. The resulting energy-level diagram is shown in Fig. 1.

This paper presents experimental data on the pressure dependence of the quartet states of Cr^{3+} in ruby: the $^4A_2 \rightarrow {}^4T_2$ and $^4A_2 \rightarrow {}^4T_1$ transition absorption bands. We have investigated these in environments of both theoretical and experimental interest: in a quasihydrostatic (QH) environment as a single crystal and a powder, and in a nonhydrostatic (NH) environment as a powder compact. The pressure dependence of the quartet states is important for several reasons. First, it is through these states that the R-line luminescence is excited in high-pressure experiments. Second, the e orbital, occupied by one of the three Cr^{3+} $3d$ electrons in a quartet state, extends in space towards the O^{2-} ligands,[12] in contrast to the t_2 orbital occupied by all three $3d$ electrons in a singlet state (from which the R and R' luminescence lines of ruby originate). Thus, the quartet states are consid-

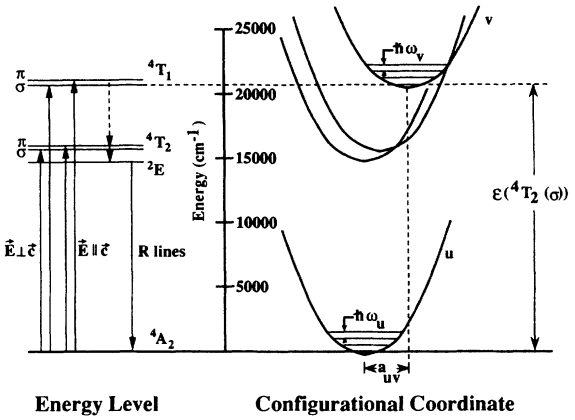

FIG. 1. Energy-level and configurational-coordinate diagrams of ruby at atmospheric pressure. In the energy-level diagram radiative transitions are solid downward arrows, and nonradiative transitions are dashed. For clarity only the σ states are shown on the configurational-coordinate diagram, and phonon states are shown only for the ground state ($^4A_2$) and the excited state $^4T_1(\sigma)$. The 29-cm^{-1} splitting between the $\overline{E}$ and $2\overline{A}$ states of ^2E state is too small to be resolved in the figure.

erably more sensitive to changes in the Cr^{3+} — O^{2-} distance due to compression,[15] making them more amenable to experimental investigation. Third, by observing the $^4T_2$, $^4T_1$, *and* ^2E state energies one can determine the crystal-field parameter Δ and the Racah parameters[12,13] B and C. The pressure dependence of the Racah parameters can be related to changes in the Cr^{3+} — O^{2-} bond covalency and, in the cubic field approximation, solely determine the R-line energy. Several experimental studies of the pressure dependence of the quartet states have been done;[16–18] however, none have measured the complete spectrum of $^4A_2\rightarrow{}^4T_2$ *and* $^4A_2\rightarrow{}^4T_1$ absorption bands, as well as the R-line luminescence.

Ideally the absorption caused by $^4A_2\rightarrow{}^4T_2$ and $^4A_2\rightarrow{}^4T_1$ transitions in ruby can be directly measured to determine the pressure dependence of these electronic levels. However, in order to obtain the pressures of this study, a DAC must be employed, requiring samples of $\leq$2500 μm^2 surface area and $\leq$30-μm thickness. With this thickness and an absorption coefficient of 7 cm^{-1} for 0.5 wt.% Cr^{3+}, there is only 2% attenuation of incident light at the maximum of an absorption band. It is difficult to measure such weak absorption accurately, especially in the spectral region where the absorption in the type-I*a* diamond anvils themselves is varying considerably. We have developed an excitation technique that eliminates this problem by observing the R-line luminescence intensity as a function of exciting wavelength in the $^4T_2$ and $^4T_1$ absorption bands. We make use of the high quantum efficiency[19] (95%) in ruby of the radiative R luminescence transitions after absorption into the quartet states and subsequent nonradiative transfer to the ^2E states. Misu [20] has shown that the excitation spectrum of ruby accurately reproduces the absorption band spectrum. The technique is similar to previous measurements;[18,21] however, our use of monochromated broadband light sources allows us to scan over the entire spectral region of the quartet absorptions, as well as compensate for diamond absorption. This complete information allows a model fit to the absorption bands and the extraction of the pressure dependence of zero-phonon lines and absorption amplitudes.

II. EXPERIMENT

Four room-temperature experiments were performed between atmospheric pressure and 30–35 GPa, as summarized in Table I. These experiments cover most of the stress environments commonly encountered in DAC experiments. Experiment 1 is particularly important since it is a single crystal in a quasihydrostatic environment, and most closely matches the conditions assumed in theoretical work. In all of the experiments type-I*a* diamond anvils with 640-μm flat tips, a stainless-steel gasket, and a 150-μm-diam sample chamber were used. Type-I*a* diamonds have a strong zero-phonon line and broadband absorption feature ($N3$) between 24 400 cm^{-1} and 28 600 cm^{-1} which must be compensated for when measuring the $^4T_1$ band. This normalization will be described below.

All ruby samples are from the same ruby boule of 0.5% Cr^{3+} by weight. The powder samples were ground to particle sizes $\leq$5 μm, and in experiment 3 constituted $\sim$25% of the sample-chamber volume. The single crystal in experiment 4 was an irregular chip approximately 50×70×30 μm^3 thick. For the single crystal in experiment 1 part of the boule was polished to 35-μm thickness. The orientation of the polished face of the boule was determined to be perpendicular to the [315] crystallographic axis (hexagonal indices) of ruby, and we estimate that after loading into the DAC the incident light **k** was parallel (within 5°) to this crystallographic axis. Argon

TABLE I. Ruby excitation experiments in the diamond anvil cell.

Experiment no.	Ruby	Pressure medium	Incident-light orientation
1	single crystal	Ar	k‖[315]
2	powder	none (ruby compact)	random
3	powder	Ar	random
4	single crystal	4:1 methanol-ethanol	unknown

was loaded into the cell as a cryogenic liquid. No bridging of the diamond anvils by the ruby chip in experiment 1 occurred as evidenced both by fringes due to interference between the polished ruby and diamond surfaces, and by an intact single crystal of ruby after decompression.

Figure 2 shows a schematic of the optical system used to measure the excitation spectra. The light source is selectable between a 150-W Xe arc lamp and a 100-W quartz tungsten halogen lamp. This beam is monochromated by a $\frac{1}{4}$-m monochromator with a 1200-grooves/mm grating blazed at 520 nm. The monochromated light passes through a field stop of 1 mm diameter, and then through a 2-mm-thick Schott BG40 filter to eliminate stray light reflections from the monochromator. This unpolarized beam is focused by half of a 15× reflecting objective through a 5-Hz chopper onto the sample. At the sample the spot size is approximately 40 μm in diameter. The reflected and luminescence beam is directed out the other half of the objective, through a 3-mm-thick Schott RG695 filter which passes only the luminescence signal, through a second 1-mm field stop, and into a GaAs phototube cooled to approximately $-30°$ C. The phototube signal is preamplified and analyzed by a lock-in amplifier. Usable signal was obtained through the monochromator filter and diamond anvil between 16 000 cm^{-1} and 30 500 cm^{-1} for the Xe source and 16 000 cm^{-1} to 23 800 cm^{-1} for the W source.

The R_1 and R_2 luminescence lines were recorded on a separate system using the 19 460-cm^{-1} line of an Ar-ion laser. The focused laser spot (~20-μm diam) was coincident with the spot on the ruby where the excitation spectrum was obtained. The luminescence light is detected by a $\frac{1}{4}$-m spectrometer with 600 grooves/mm blazed at 700 nm, and an EG&G 1454 OMA diode array. This system has a resolution of 9 cm^{-1} at the ruby R lines. A least-squares-fitting routine was used to deconvolve the R-line luminescence data into two Gaussian peaks. This was particularly important in experiment 2 (ruby compact) where the luminescence lines broadened considerably.[22] Pressures are based on the nonhydrostatic R_1-line calibration[4] for experiment 2, and on the quasihydrostatic calibration[5] for the other experiments, although in the pressure range of this study the difference between the two calibrations is less than 1 GPa. In each system the exciting light enters and the luminescence light exits perpendicular to the anvil flat.

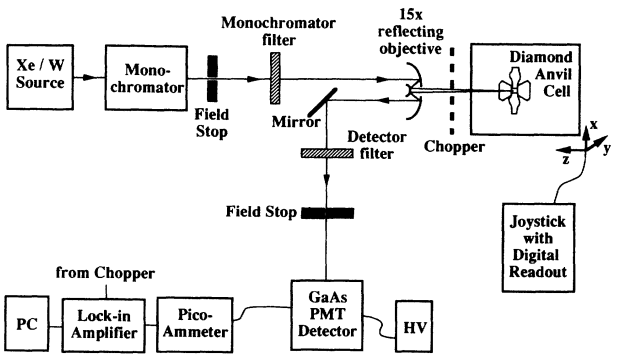

FIG. 2. Schematic diagram of the high-pressure excitation experiment.

III. ANALYSIS

A. Spectrum normalization

As mentioned previously, it is important to compensate the excitation spectra for the wavelength dependence of absorption in the diamond anvils. Also the spectra must be normalized to the source spectrum, monochromator filter response, and detector response. This normalization will now be described.

The signal detected by the photomultiplier tube, $P(\tilde{\nu})$, as a function of the monochromator wave number $\tilde{\nu}$, is

$$P(\tilde{\nu}) = C_1 I_0(\tilde{\nu}) T_M(\tilde{\nu}) e^{-t\alpha_d(\tilde{\nu})} \times E(\tilde{\nu}) e^{-t\alpha_d(\tilde{\nu}_R)} T_D(\tilde{\nu}_R) D(\tilde{\nu}_R) , \quad (4)$$

where C_1 is a geometrical constant independent of wave number, $I_0(\tilde{\nu})$ the source spectrum intensity that exits the monochromator, $T_M(\tilde{\nu})$ the transmission of the monochromator filter, t the diamond thickness, $\alpha_d(\tilde{\nu})$ the diamond absorption coefficient, $\tilde{\nu}_R$ the ruby R luminescence wave number, $T_D(\tilde{\nu})$ the detector filter transmission, and $D(\tilde{\nu})$ the detector response. The intensity of emitted R luminescence light when the ruby is excited by light of wave number $\tilde{\nu}$ is $E(\tilde{\nu})$, the ruby excitation signal. Equation (4) neglects the light reflected off the ruby and diamond surfaces since this is completely absorbed by the detector filter. Note that for an excitation spectrum at a given pressure the terms to the right of $E(\tilde{\nu})$ are constants, and Eq. (4) can be written

$$P(\tilde{\nu}) = C_2 I_0(\tilde{\nu}) T_M(\tilde{\nu}) e^{-t\alpha_d(\tilde{\nu})} E(\tilde{\nu}). \quad (5)$$

The excitation spectrum, $E(\tilde{\nu})$, is determined by normalizing these data. A normalization curve, $N(\tilde{\nu})$, is collected as an atmospheric pressure absorption spectrum of the single diamond anvil through which the incident light passes in the excitation experiment. This is done by removing the sample and gasket, the opposing diamond anvil, and the detector filter, and positioning the detector on the opposite end of the DAC from which the light enters. This curve is given by

$$N(\tilde{\nu}) = C_3 I_0(\tilde{\nu}) T_M e^{-t\alpha_d(\tilde{\nu})} D(\tilde{\nu}), \quad (6)$$

where C_3 is a third wave-number-independent constant that includes losses due to reflection at the diamond-air interfaces. Dividing Eq. (5) by Eq.(6) yields

$$\frac{P(\tilde{\nu})}{N(\tilde{\nu})} = C_4 \frac{E(\tilde{\nu})}{D(\tilde{\nu})}. \quad (7)$$

Finally, this result is multiplied by the detector response given by[23],

$$\log_{10}[D(\tilde{\nu})] = \frac{1620}{\tilde{\nu}} - 0.1455$$

$$(33\,300\ \text{cm}^{-1} \leq \tilde{\nu} \leq 11\,100\ \text{cm}^{-1}) \quad (8)$$

which gives a result proportional to the excitation spectra. This normalization assumes that the diamond absorption remains constant as the pressure is increased, which is considered reasonable for the pressures attained in this study.

B. Electronic transition parameters

Due to the coupling in ruby of the quartet states to the lattice, these excited states are modified by strains due to phonons. In fact, for the $^4A_2 \rightarrow {}^4T_2$ and $^4A_2 \rightarrow {}^4T_1$ transitions in ruby at room temperature, the absorption (or excitation) spectra show no sharp feature corresponding to the unmodified zero-phonon-line (ZPL) transition.[20] Since most theoretical treatments determine ZPL energies, and the R lines themselves are ZPL's, we want to extract the pressure dependence of the quartet state ZPL energies from the excitation data. Further, we want to determine the pressure dependence of the lattice coupling in order to understand the pressure variation of phenomena that are related to this coupling, such as nonradiative transition probabilities and absorption band shapes.[24]

To extract the ZPL's and lattice coupling parameters, we use a method similar to that used by Eggert, Goettel, and Silvera.[18] The quantum-mechanical single-configurational-coordinate model (QMSCC) of Struck and Fonger[24] is used to calculate the absorption band shape of ruby.[25] The ruby configurational-coordinate diagram is shown in Fig. 1. Each excited state v or ground state u is modeled by a phonon spectrum consisting of a single phonon frequency ω_v or ω_u, respectively. Each *pair* of states is characterized by a Franck-Condon offset between the parabola minima, a_{uv} (in units of zero-point-vibration amplitude), and a ZPL energy difference, $\mathcal{E}(u \rightarrow v)$. The Manneback angle θ for the transition is defined as[24]

$$\theta \equiv \arctan\left(\frac{\hbar\omega_v}{\hbar\omega_u}\right)^{1/2} \quad (9)$$

For the quartet absorption bands in ruby the ground state, u, is always $^4A_2$ while there are four excited states, v: $^4T_2(\sigma)$, $^4T_2(\pi)$, $^4T_1(\sigma)$, and $^4T_1(\pi)$. The σ states are excited by light with $\mathbf{E}\perp\mathbf{c}$ and the π states with $\mathbf{E}\|$ c. The 14 QMSCC and data acquisition parameters needed, in general, to be fitted to the ruby absorption data are given in Table II. The amplitudes a_1, a_2, a_3, and a_4 include the $u \rightarrow v$ transition probablility, the quantum efficiency, and an experimental factor due to C_4 in Eq. (7). For ruby, the Manneback angle θ is the same for all four transitions.[25] A small wave-number-independent offset b is added to the calculated spectrum to account for stray light. The a_{uv} and ω_v are considered the same for both σ and π transitions within the same quartet state.

The 14 parameters of Table II are reduced to seven pressure-dependent ones by the following assumptions and calculations.

The Manneback angle θ, Eq. (9), is related to the ratio of ground- and excited-state phonon energies, each of which are expected to have similar dependencies on pressure. Therefore, θ is considered constant at the atmospheric pressure value[25] of 44°.

The ratios a_1/a_2 and a_3/a_4 are known from single-crystal studies with polarized light.[20] In experiments 1 through 3 the relative intensities of σ and π transitions can be calculated for the unpolarized incident light by averaging over all polarizations (assuming a random orientation in the powder experiments). Therefore a_2 can be calculated from a_1, and a_4 from a_3. This is not known for experiment 4 since the orientation of the irregular chip was not determined.

The ZPL energy differences $\mathcal{E}[^4T_2(\pi)] - \mathcal{E}[^4T_2(\sigma)]$ and $\mathcal{E}[^4T_1(\pi)] - \mathcal{E}[^4T_1(\sigma)]$ can be estimated from energy differences between the R_1 and R_2 luminescence lines. For this we assume[26] that the R_1,R_2 splitting is proportional to k, the trigonal-field-splitting parameter [Eq. (2)], and that k' is constant with pressure. Macfarlane[13] has shown that, for ruby,

$$\mathcal{E}[^4T_2(\pi)] - \mathcal{E}[^4T_2(\sigma)] = \frac{k}{2}$$

and (10)

$$\mathcal{E}[^4T_1(\pi)] - \mathcal{E}[^4T_1(\sigma)] = \frac{k}{2} + k'.$$

TABLE II. QMSCC and data acquisition parameters for the $^4T_2$ and $^4T_1$ absorption bands in ruby. These 14 parameters can be reduced to seven pressure-dependent variables as discussed in Sec. III B.

Parameter	Symbol			
Zero-phonon-line energy	$\mathcal{E}[^4T_2(\sigma)]$	$\mathcal{E}[^4T_2(\pi)]$	$\mathcal{E}[^4T_1(\sigma)]$	$\mathcal{E}[^4T_1(\pi)]$
Band amplitude	a_1	a_2	a_3	a_4
Excited-state phonon frequency	$\omega_v(^4T_2)$		$\omega_v(^4T_1)$	
Franck-Condon offset	$a_{uv}(^4T_2)$		$a_{uv}(^4T_1)$	
Manneback angle	θ			
Data offset	b			

By scaling the atmospheric pressure value of $k_0 = 800$ cm^{-1} with the measured R_1,R_2 splitting, and using the constant value[13] $k' = 400$ cm^{-1}, we can determine these ZPL energy differences.

The nine remaining parameters ($\mathcal{E}[^4T_2(\sigma)]$, $\mathcal{E}[^4T_1(\sigma)]$, a_1,a_3,$\omega_v(^4T_1)$,$\omega_v(^4T_2)$, $a_{uv}(^4T_1)$, $a_{uv}(^4T_2)$, and b) were least-squares fitted to three excitation spectra taken at low pressures (<1 GPa). By averaging the phonon-frequency results we obtain initial values of $\omega_{v0}(^4T_2)=491\pm13$ cm^{-1} and $\omega_{v0}(^4T_1)=504\pm12$ cm^{-1}. These values are in excellent agreement with the 500 cm^{-1} determined for ruby by Fonger and Struck.[25] The excited-state phonon frequencies are then removed from the parameter list by linearly scaling them with pressure using the Al_2O_3 Grüneisen parameter[27,18] $\gamma = 1.310$:

$$\omega_v = \omega_{v0} + \left(\frac{d\omega_v}{dP}\bigg|_{P=0}\right)P = \omega_{v0} + \frac{\omega_{v0}}{B_0}\gamma P, \qquad (11)$$

where $B_0 = 253$ GPa is the bulk modulus of ruby[28] and P the pressure.

C. Crystal-field and Racah parameters

In the cubic crystal-field approximation the ZPL energies are given by[12,29]

$$\mathcal{E}(^4A_2 \rightarrow {}^4T_2) = \Delta ,$$

$$\mathcal{E}(^4A_2 \rightarrow {}^4T_1) = \tfrac{1}{2}[3\Delta + 15B - (\Delta^2 - 18B\Delta + 225B^2)^{1/2}],$$

$$\mathcal{E}(^4A_2 \rightarrow {}^2E) = 9B + 3C. \qquad (12)$$

where Δ is the crystal-field-splitting parameter, and B and C are Racah parameters. If the O^{2-} ligands are modeled as point charges $-Ze$ at a distance a in the cubic symmetry (O_h), then the crystal-field-splitting parameter is[12]

$$\Delta = \frac{70}{42}\frac{Ze^2\langle r^4\rangle_{3d}}{a^5} , \qquad (13)$$

where $\langle r^4\rangle_{3d} = \int dr\, r^6 \mid R_{3d}(r) \mid^2$ and $R_{3d}(r)$ is the radial part of the Cr^{3+} $3d$ electronic state. If we assume Z and $\langle r^4\rangle_{3d}$ remain constant with pressure, then the volume dependence of Δ will be[16] $V^{-5/3}$. We point out that the power of a in Eq. (13), and therefore the power of V, will depend on the ligand charge distribution. For example, replacing the point charges with dipoles results[12] in a^6 in the denominator of Eq. (13).

In experiments 1 and 3 we have all three transition energies in Eq. (12), and therefore can determine Δ, B, and C to 35 GPa. Experiment 2 yielded only the $^4A_2 \rightarrow {}^4T_2$ transition and Δ. In all cases the cubic field ZPL's were determined from the measured full trigonal field ZPL's using an average weighted by the ZPL degeneracy:

$$\mathcal{E}(^4T_2) = \tfrac{1}{3}\{2\mathcal{E}[^4T_2(\sigma)] + \mathcal{E}[^4T_2(\pi)]\} ,$$

$$\mathcal{E}(^4T_1) = \tfrac{1}{3}\{2\mathcal{E}[^4T_1(\sigma)] + \mathcal{E}[^4T_1(\pi)]\} , \qquad (14)$$

$$\mathcal{E}(^2E) = \tfrac{1}{2}\left[\mathcal{E}(2\overline{A}) + \mathcal{E}(\overline{E})\right] ,$$

where $\mathcal{E}(^4T_2)$ represents the ZPL energy of the $^4A_2 \rightarrow {}^4T_2$ transition. It is important to recognize that Δ, B, and C are calculated from the ZPL energies and *not* the energy of the absorption band maximum. The energy of this maximum can be approximated by the first moment of the band which is given by[25]

$$E_{max} \simeq E_{ZPL} + \tfrac{1}{2}\hbar\omega_v a_{uv}^2 \sin^2\theta \qquad (15)$$

where E_{ZPL} is the ZPL energy. Since there is no *a priori* reason to assume a_{uv} is constant with pressure, and $\hbar\omega_v$ varies as given in Eq. (11), the use of E_{max} to calculate the pressure dependence of Δ, B, and C may lead to systematic errors.

IV. RESULTS

We first present results from experiment 1, a single-crystal ruby sample in an Ar quasihydrostatic pressure environment. Figure 3 contrasts the $^4A_2 \rightarrow {}^4T_2$ and $^4A_2 \rightarrow {}^4T_1$ excitation and R-line luminescence spectra at low pressure (3.7 GPa) and high pressure (34 GPa). The blue shifts of the quartet states are approximately an order of magnitude greater than the R-line red shifts. Also shown in the figure are the fits to the QMSCC model, which are seen to be successful over the entire pressure range of the study. Figure 4 shows the pressure dependence of $\mathcal{E}(^4T_2)$ and $\mathcal{E}(^4T_1)$, respectively. These data for the quasihydrostatic environment are well characterized by a linear dependence on pressure:

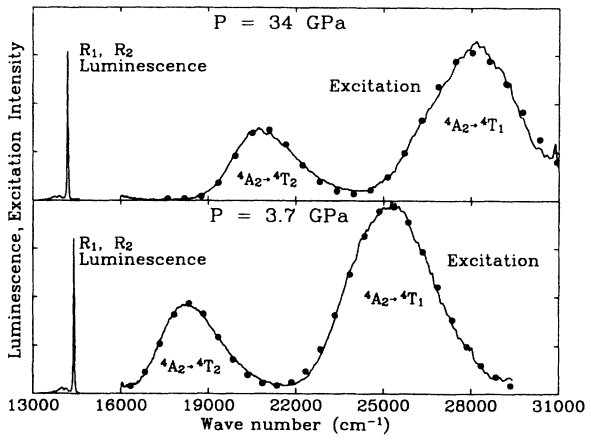

FIG. 3. Comparison of the room-temperature ruby R_1 and R_2 luminescence and excitation signal at 3.7 GPa and 34 GPa in experiment 1. For the excitation signal the solid line is the data, and the points are the results of the QMSCC model fits.

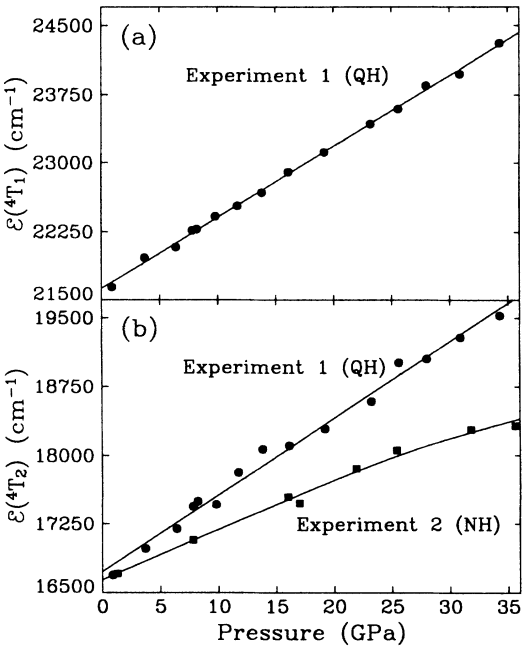

FIG. 4. (a) Values of $\mathcal{E}(^4T_1)$ in the cubic approximation [Eq. (14)] for the quasihydrostatic experiment 1. (b) Values of $\mathcal{E}(^4T_2)$ for experiment 1 (circles), and the nonhydrostatic experiment 2 (squares). For experiment 1 the data are fit to straight lines with parameters given in Eq. (16), and for experiment 2 the line through the data is a guide to the eye.

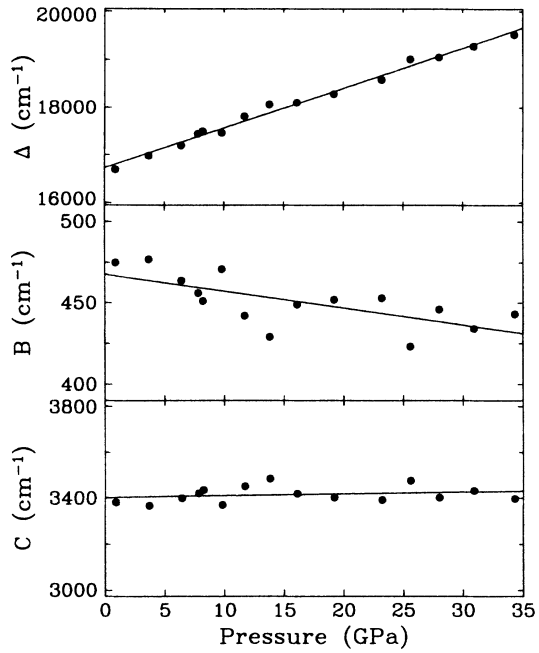

FIG. 5. The pressure dependence of the crystal-field-splitting parameter Δ and Racah parameters B and C in the quasihydrostatic experiment 1. The parameters of the straight-line fits through the data are given in Eq. (17). As an aid in observing relative shifts, the range of each ordinate is 25% of the parameter's atmospheric pressure value.

$$\mathcal{E}(^4T_2) = (16\,730 \pm 50) + (84 \pm 3)P \ ,$$
$$\mathcal{E}(^4T_1) = (21\,630 \pm 20) + (78 \pm 1)P, \tag{16}$$

where P is in GPa, and $\mathcal{E}(^4T_2)$ and $\mathcal{E}(^4T_1)$ are in cm^{-1}. The atmospheric pressure ZPL energies are in good agreement with those determined by Fonger and Struck[25] (16 620 cm^{-1} for $^4T_2$ and 21 580 cm^{-1} for $^4T_1$).

The Franck-Condon offsets $a_{uv}(^4T_2)$ and $a_{uv}(^4T_1)$ are only slightly affected in the quasihydrostatic pressure environment to 35 GPa: $a_{uv}(^4T_2)$ has decreased by ~5% from 3.59 at atmospheric pressure and $a_{uv}(^4T_1)$ has increased by ~2% from 5.25. The resulting changes at 35 GPa are approximately the magnitude of the scatter in the data. The atmospheric pressure a_{uv} values are in good agreement with those determined by Fonger and Struck[25] [3.53 and 5.23 for $a_{uv}(^4T_2)$ and $a_{uv}(^4T_1)$, respectively]. No significant changes were observed in either the absolute excitation signal amplitudes or the ratio of the $^4T_2$ amplitude to the $^4T_1$ amplitude (a_1/a_3).

The pressure dependencies of Δ, B, and C as determined from Eq. (12) are shown in Fig. 5. The data are satisfactorily fitted by a linear dependence on pressure:

$$\Delta = (16\,730 \pm 50) + (84 \pm 3)P \ ,$$
$$B = (468 \pm 6) - (1.1 \pm 0.3)P \ , \tag{17}$$
$$C = (3402 \pm 17) + (0.8 \pm 0.9)P \ ,$$

where each parameter is in cm^{-1} and P is in GPa. Δ has increased by 18% at 35 GPa, B has decreased by 7.5%, and C remains constant within the scatter of the data. The ratio B/C therefore decreases by 7.5% between atmospheric pressure and 35 GPa, a result in contrast to the constant B/C assumed in most theoretical work.[30,31,15] These results will be discussed more fully in the next section.

We turn now to experiment 2, a ruby powder compact in a nonhydrostatic environment. Fit results of $\mathcal{E}(^4T_2)$ for this experiment are shown in Fig. 4 along with those for the quasihydrostatic experiment. The nonhydrostatic data show a considerably smaller increase with pressure, and nonlinearity at the highest pressures. In fact, the value of $\mathcal{E}(^4T_2)$ at 35.6 GPa of 18 320 cm^{-1} represents a 1590-cm^{-1} change from the atmospheric pressure value, only half as great as the change in the quasihydrostatic case. It is noted that in shock experiments,[17,32] which are expected to be nonhydrostatic, the absorption band maximum is found at a lower wave number than would be expected from a linear extrapolation of the hydrostatic part of the static data of Stephens and Drickamer.[16] The measured band maximum at 31.8 GPa in our nonhydrostatic experiment is 20 000±100 cm^{-1} which agrees with the shock result of 19 600±200 cm^{-1} at 30.1± 0.5 GPa.[17] The low pressure static data of Ref. 16 also show a bendover at ~7.5 GPa in $\mathcal{E}[^4T_2(\sigma)]$ and $\mathcal{E}[^4T_1(\sigma)]$ which has been attributed to nonhydrostatic stresses.[26] These results are all consistent with our observation that $\mathcal{E}(^4T_2)$ (and therefore Δ) depend significantly on the state of

stress.

Although the scatter in $a_{uv}(^4T_2)$ in experiment 2 is approximately twice that of experiment 1, we are able to see a difference in this parameter also. While there was only a slight decrease in $a_{uv}(^4T_2)$ in the quasihydrostatic case, there is an increase in the nonhydrostatic case. At 35 GPa a_{uv}=3.94±0.15, a 12% increase over the atmospheric pressure value[25] of 3.53. A small part of this increase may be due to pressure gradients over the 40-μm area sampled in the excitation spectra, which would effectively broaden the absorption band. From Eq. (15) we see that a_{uv} is related to the bandwidth, defined in this case as the difference between the ZPL energy and the band maximum. From the R_1 luminescence measurements at 32 GPa we estimate a 1.5 GPa gradient over the 40-μm spot, which corresponds to a 120-cm^{-1} shift in the $^4T_2$ ZPL energy. Using this shift as an estimate of the amount of broadening of the $^4T_2$ band this gradient would cause, Eq. (15) gives a 1.5% increase in $a_{uv}(^4T_2)$, not enough to explain the measured increase. By a similar argument the pressure gradient cannot explain the dramatic differences in the $\mathcal{E}(^4T_2)$ ZPL energy between the quasihydrostatic and nonhydrostatic experiments. Between atmospheric pressure and ~10 GPa the $^4T_2$ amplitude increased fivefold due to the closing of voids and reduction of grain-boundary scattering. Above 10 GPa the nonhydrostatic experiment showed no significant changes in the excitation amplitude of the $^4T_2$ band, the same behavior observed in the quasihydrostatic experiment.

Finally, we discuss the results of experiments 3 and 4. The QMSCC model fits to the quasihydrostatic powder data of experiment 3 show no deviation from the single-crystal data, with the exception of a small (-200 cm^{-1}) constant offset of the $\mathcal{E}(^4T_1)$ ZPL energy, the origin of which is not known. Otherwise the pressure dependence of ZPL energies, a_{uv}'s, and amplitude data in experiments 1 and 3 agree within experimental error. This eliminates the possibility that the large differences in $\mathcal{E}(^4T_2)$ observed for experiment 2 were due to the powder nature of the sample. Since the orientation of the single crystal in 4:1 methanol-ethanol (experiment 4) is unknown a complete analysis is not possible. However, the $^4T_2$-band excitation data qualitatively agree with that of the quasihydrostatic experiments 1 and 3.

V. DISCUSSION

A. Quasihydrostatic pressure dependence of Δ, B, and C

From the discussion after Eq. (13), the point-charge model in the cubic approximation predicts $\Delta \propto V^{-5/3}$. Figure 6 shows a plot of $\log_{10}(\Delta/\Delta_0)$ versus $\log_{10}(V_0/V)$ for the quasihydrostatic single-crystal data. The fractional volume V/V_0 has been calculated from the Birch-Murnaghan[33] equation of state using[28] B_0 = 253 GPa and B_0' = 5.0. The measured data fall systematically below the line with slope $\frac{5}{3}$ predicted by the point-charge model. The fitted slope of these data is 1.50 ± 0.02.

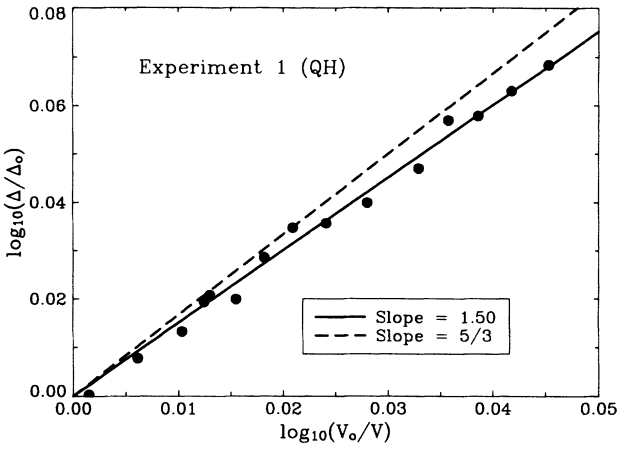

FIG. 6. Log-log plot of the reduced crystal-field-splitting parameter (Δ/Δ_0) versus the inverse of the reduced volume (V/V_0) for the quasihydrostatic experiment 1. The solid line is a fit to the data with an intercept of zero and slope 1.50 ± 0.02. The dashed line has slope $\frac{5}{3}$, as predicted by the point-charge model [Eq. (13)].

This failure of the model has been rectified in the literature in two ways. First, the theories of Munro[15] and Eggert *et al.*,[18] use pressure and volume, respectively, to scale the electronic charge (e) and nuclear charge number (Z) of Eq. (13). The values of $d\mathcal{E}(^4T_2)/dP$ calculated by the two methods give 97 cm^{-1}/GPa for pressure scaling[15] and ~ 74 cm^{-1}/GPa for volume scaling.[18] Equation (13) without scaling yields 110 cm^{-1}/GPa. The addition of scaling improves the agreement with our measured quasihydrostatic slope of 84±3 cm^{-1}/GPa. We note that inclusion of the anticrossing theory[18] due to interactions between the $^4T_2$ and $^2T_2$ states would not improve the agreement with the volume scaling theory. At 35 GPa we do not expect such interactions to play a critical role in determining the $^4T_2$ level energy.

Second, the cubic field point charge model prediction for Δ [see Eq. (13)] can be kept in its entirety if the lower measured slope in Fig. 6 is a result of lower compressibility of the Cr^{3+} site compared to the bulk Al_2O_3 lattice. Using a bulk modulus of 320 GPa brings the data of Fig. 6 to a slope of $\frac{5}{3}$. It has been pointed out[17] that if the substituting ion is larger than the host, then the local compressibility will be lower. This is the case for ruby where[34] $r_{Al^{3+}}$ = 0.53 Å and $r_{Cr^{3+}}$ = 0.615 Å. Our data indicate that the local Cr^{3+} compressibility is lower than the bulk at *all* pressures, not just at volume compressions greater than 6% as suggested earlier.[17] The earlier conclusion was based on a combination of hydrostatic[16] and nonhydrostatic[17] data.

As shown in Eq. (12) the R luminescence energy in the cubic crystal-field approximation is given by the Racah parameters B and C. The measured values of these parameters indicate that the primary contribution to the pressure dependence of the R lines is through B. Of

course, a full analysis must include the effects of the trigonal part of the crystal field, $\mathcal{H}_{\text{trig}}$, and $\mathcal{H}_{\text{SO}}$.

B. Nonhydrostatic pressure dependence of $\mathcal{E}(^4T_2)$

Our data indicate a significant dependence of $\mathcal{E}(^4T_2)$ on the state of stress experienced by the Cr^{3+} ion. The analysis of this dependence is complicated by several factors. First, the nonhydrostatic state may result in crystal fields deviating significantly from cubic symmetry. The lowering of this symmetry will result in further splittings of the quartet states and a more complicated interpretation of the absorption spectrum. Such effects have been observed in shock experiments below the Hugoniot elastic limit.[35] Second, the existence of shear stresses will introduce nonisotropic changes in the crystal field. Details of the resulting changes in the O^{2-} $2p$ orbital overlap with the Cr^{3+} $3d$ orbitals, completely ignored in the point-charge model, may become important.

Irrespective of the source, the differences in $\mathcal{E}(^4T_2)$ during quasihydrostatic and nonhydrostatic loading influence several other properties of the Cr^{3+} electronic spectrum. For example, the ^2E state interacts with the $^4T_2$ state through the spin-orbit contribution $\mathcal{H}_{\text{SO}}$ to the full $3d$-electron Hamiltonian. Since the spin-orbit contribution to the energy is much smaller than that of the crystal field, we use perturbation theory to estimate the interaction. To first order there is no interaction[12] since $\langle ^2E \mid \mathcal{H}_{\text{SO}} \mid ^2E\rangle = 0$. To second order the perturbation of the ^2E state is

$$\Delta\mathcal{E}(^2E) = \frac{|\langle ^2E \mid \mathcal{H}_{\text{SO}} \mid ^4T_2\rangle|^2}{\mathcal{E}(^2E) - \mathcal{E}(^4T_2)} , \tag{18}$$

where[14] $|\langle ^2E|\mathcal{H}_{\text{SO}}|^4T_2\rangle|^2 = |-4i\zeta'|^2 \simeq 3.1\times 10^5\ (\text{cm}^{-1})^2$. Our data indicate that there are significant differences in the denominator of Eq. (18) between the quasihydrostatic and nonhydrostatic conditions. Evaluating the difference in the perturbation in the two cases at 35 GPa, we get a difference in $\mathcal{E}(^2E)$ (the R-line mean energy) of

$$\Delta\mathcal{E}_{\text{QH}}(^2E) - \Delta\mathcal{E}_{\text{NH}}(^2E) = 17\ \text{cm}^{-1}\ \ (35\ \text{GPa}) , \tag{19}$$

where QH and NH refer to quasihydrostatic and nonhydrostatic environments, respectively. At 35 GPa the difference in the QH and NH R_1-line calibrations[3,5] is approximately 6 cm^{-1}. Although this is a small effect at this pressure, the difference in perturbation of the ^2E level by the $^4T_2$ level under different states of stress is of the same sign and order of magnitude, and clearly plays a role in explaining the difference in the two calibrations. The nonhydrostaticity of our ruby compact is expected to be greater than that generated in the nonhydrostatic calibration where the ruby was mixed with metallic pressure markers,[3,4] possibly explaining the larger deviation observed here. In addition to this effect the influence of nonhydrostatic stresses on the x-ray diffraction results used in the calibration must also be considered. A complete analysis will require a better understanding of the states of stress generated in the DAC, as well as a more accurate evaluation of ζ' in Eq. (3).

The measured difference of $\mathcal{E}(^2E)-\mathcal{E}(^4T_2)$ under QH and NH states of stress will also influence the R-line lifetime, τ. Sharma and Gupta[36] have obtained an expression for the oscillator strength of the $^2E \rightarrow {}^4A_2$ transition which can be related to the R-line lifetime by

$$\tau \propto \frac{1}{f} = \frac{27\hbar^2}{16\pi^2 m}\left(\frac{[\mathcal{E}(^2E) - \mathcal{E}(^4T_2)]^2}{\mathcal{E}(^2E)\zeta'^2 \mid P_{\text{eff}} \mid^2}\right) \tag{20}$$

where $\mid P_{\text{eff}} \mid^2$ is the effective electric dipole transition moment for $^2E \rightarrow {}^4A_2$ transitions. When we evaluate the state of stress dependence of the numerator of Eq. (20) at 35 GPa we have

$$\frac{\tau_{\text{QH}} - \tau_{\text{NH}}}{\tau_{\text{NH}}} \sim 40\%. \tag{21}$$

Scatter of this magnitude has been observed in the lifetime experiments of Eggert *et al.*[11] and has been attributed to the probing of ruby crystallites in different states of stress. We see that this stress dependence can be entirely ascribed to the differences in $\mathcal{E}(^2E) - \mathcal{E}(^4T_2)$. This implies that the product $\mathcal{E}(^2E)\zeta'^2 \mid P_{\text{eff}} \mid^2$ is relatively insensitive to nonhydrostatic states of stress.

C. Excitation of R lines for pressure measurement

Figure 3 shows that the $^4T_2$ and $^4T_1$ states and their associated phonon sidebands move to higher energy rapidly with pressure. At 35 GPa there is no indication that the efficiency of excitation through either of these bands is diminishing significantly with pressure. The problem with excitation at higher pressures is due to the movement of these bands away from the Ar-ion laser lines used to excite the luminescence. However, the normalized data presented in Fig. 3 are deceiving for DAC use since diamond absorption needs to be considered. For example, it would appear that excitation through $^4T_1$ would be $\sim$2 times as efficient as through $^4T_2$. However, even at 35 GPa the $^4T_1$ band has moved sufficiently far into the $N3$ absorption of the type Ia diamond anvils[37] to render it less efficient for R-line excitation than the $^4T_2$ band.

Also, since the $^4T_2$ band does not move as quickly in the nonhydrostatic case we expect rubies in this stress environment to be more efficiently excited with an Ar-ion laser than ruby chips in a more hydrostatic environment. This effect is in addition to the greater R-line intensity in a nonhydrostatic environment due to a shorter lifetime and resulting greater R-line intensity at power saturation.[11]

Finally, grain-boundary scattering can be an important mechanism for loss of efficiency of excitation and detection of the R luminescence in the DAC. In the nonhydrostatic ruby powder experiment the excitation signal increased by a factor of 5 between atmospheric pressure and 10 GPa as the intergrain voids were closed. If, at extreme pressures, a ruby crystal originally loaded as a

single crystal breaks due to bridging we expect the luminescence signal to decrease. This may become especially significant on unloading as voids are formed.

VI. CONCLUSIONS

We have shown that excitation spectroscopy in the diamond anvil cell can be used to study the pressure dependence of absorption features that are too weak to study directly. For the case of Cr^{3+} in ruby, the following conclusions can be drawn for the ${}^4A_2 \rightarrow {}^4T_2$ and ${}^4A_2 \rightarrow {}^4T_1$ transition ZPL's and phonon side bands.

In a quasihydrostatic medium $\mathcal{E}({}^4T_2)$ and $\mathcal{E}({}^4T_1)$, and therefore Δ, depend linearly on pressure to 35 GPa. The Racah parameter B shows a 12% decrease, and C shows no significant change. The amplitudes and Franck-Condon offsets of the QMSCC model do not vary with pressure for either of the two transitions.

The pressure dependence of $\mathcal{E}({}^4T_2)$ for ruby in a nonhydrostatic environment shows very different behavior. It has a 34% smaller slope at low pressure, and a bendover at the highest pressures, implying a difference in the effects of the O^{2-} crystal field in this environment. Therefore theories that do not explicitly take into account the effects of nonhydrostatic stresses should not be expected to explain a combination of data taken under different conditions of stress.[30] While the excitation amplitude of the ruby compact remained constant after the closure of voids, the Franck-Condon offset increased ~15% between atmospheric pressure and 35 GPa.

The prediction of the cubic crystal-field point-charge model that $\Delta \propto V^{-5/3}$ is not satisfied if V is interpreted as the volume of the Al^{3+} site in the bulk crystal. For the quasihydrostatic data Δ is proportional to $V^{-3/2}$. If the Cr^{3+} site bulk modulus is modeled as 320 GPa (28% greater than that of the bulk crystal), then the $V^{-5/3}$ prediction is satisfied.

The difference in $\mathcal{E}({}^4T_2)$ between quasihydrostatic and nonhydrostatic loading influences other properties of the ruby spectrum. We have shown that through spin-orbit coupling this can become a significant factor in determining the R_1 line calibration difference between these states of stress. Similarly, the R-line lifetime will be shorter in a nonhydrostatic environment due to an increase in the oscillator strength resulting from increased mixing of the ${}^4T_2$ and ${}^2E$ states since their energy levels are closer together.

Since the amplitude of the excitation signal remains constant and the bands do not broaden significantly with pressure, we conclude that the band movement away from the Ar-ion laser lines is primarily responsible for the decrease in R-line integrated intensity as the pressure is increased. Also, significant broadening of the luminescence R lines themselves will reduce the measured peak height.

ACKNOWLEDGMENTS

We thank Serge Desgreniers for assistance in developing the excitation setup. One of us (S.J.D.) thanks AT&T Bell Laboratories for support. This work received support from the National Science Foundation through Grant No. DMR-86-12289.

*Present address: AT&T Bell Laboratories, 600 Mountain Ave., Murray Hill, NJ 07974.
[1] J. D. Barnett, S. Block, and G. J. Piermarini, Rev. Sci. Instrum. **44**, 1 (1973).
[2] A. Jayaraman, Rev. Mod. Phys. **55**, 65 (1983).
[3] P. M. Bell, Ji-an Xu, and H. K. Mao, in *Shock Waves in Condensed Matter*, edited by Y. M. Gupta (Plenum, New York, 1985), p. 125.
[4] H. K. Mao, P. M. Bell, J. W. Shaner, and D. J. Steinberg, J. Appl. Phys. **49**, 3276 (1978).
[5] H. K. Mao, J. Xu, and P. M. Bell, J. Geophys. Res. **91**, 4673 (1986).
[6] K. Asaumi and A. L. Ruoff, Phys. Rev. B **33**, 5633 (1986).
[7] D. M. Adams, R. Appleby, and S. K. Sharma, J. Phys. E **9**, 1140 (1976).
[8] Yogesh K. Vohra, Steven J. Duclos, Keith E. Brister, and Arthur L. Ruoff, Phys. Rev. Lett. **61**, 574 (1988).
[9] H. K. Mao and R. J. Hemley, Science **244**, 1462 (1989).
[10] Yosiko Sato-Sorensen, J. Appl. Phys. **60**, 2985 (1986).
[11] Jon H. Eggert, Kenneth A. Goettel, and Isaac F. Silvera, Phys. Rev. B **40**, 5733 (1989).
[12] Satoro Sugano, Yukito Tanabe, and Hiroshi Kamimura, *Multiplets of Transition-Metal Ions in Crystals* (Academic, New York, 1970).
[13] R. M. Macfarlane, J. Chem. Phys. **39** , 3118 (1963).
[14] Satoru Sugano and Yukito Tanabe, J. Phys. Soc. Jpn. **13**, 880 (1958).
[15] R. G. Munro, J. Chem. Phys. **67**, 3146 (1977).
[16] D. R. Stephens and H. G. Drickamer, J. Chem. Phys. **35**, 427 (1961).
[17] Tsuneaki Goto, Thomas J. Ahrens, and George R. Rossman, Phys. Chem. Minerals **4**, 253 (1979).
[18] Jon H. Eggert, Kenneth A. Goettel, and Isaac F. Silvera, Phys. Rev. B **40**, 5724 (1989).
[19] R. S. Quimby and W. M. Yen, J. Appl. Phys. **51**, 1780 (1980).
[20] Akira Misu, J. Phys. Soc. Jpn. **19**, 2260 (1964).
[21] Richard A. Forman, Bernard A. Weinstein, and Gasper Piermarini, in *Colloque International du C.N.R.S., Spectroscopie des Éléments de Transition et des Éléments Lourds dans les Solides No. 255* (Centre National de la Recherche Scientifique, Paris, 1977), p. 51.
[22] R. G. Munro, G. J. Piermarini, S. Block, and W. B. Holzapfel, J. Appl. Phys. **57**, 165 (1985).
[23] Dennis P. Strommen and Kazuo Nakamoto, *Laboratory Raman Spectroscopy* (Wiley, New York, 1984).
[24] C. W. Struck and W. H. Fonger, J. Lumin. **10**, 1 (1975).
[25] W. H. Fonger and C. W. Struck, Phys. Rev. B **11**, 3251 (1975).
[26] Surinder M. Sharma and Y. M. Gupta, Phys. Rev. B **40**,

3329 (1989).
[27] E. Schreiber and O. L. Anderson, J. Am. Ceram. Soc. **49**, 184 (1966).
[28] Pascal Richet, Ji-An Xu, and Ho-Kwang Mao, Phys. Chem. Minerals **16**, 207 (1988).
[29] R. M. Macfarlane, J. Chem. Phys. **47**, 2066 (1967).
[30] Ma Dong-ping, Wang Zhao-qing, Chen Ju-rong, and Zhang Zheng-gang, J. Phys. C **21**, 3585 (1988).
[31] Zhao Min-Guang, Xu Ji-An, Bai Gui-Ru, and Xie Huong-Sen, Phys. Rev. B **27**, 1516 (1983).
[32] R. S. Hixson, P. M. Bellamy, G. E. Duvall, and C. R. Wilson, in *Shock Waves in Condensed Matter—1981*, Proceedings on the Conference on Shock Waves in Condensed Matter, AIP Conf. Proc. No. 78, edited by W. J. Nellis, L. Seaman, and R. A. Graham (A.I.P., New York, 1982), p. 282.
[33] F. Birch, J. Geophys. Res. **83**, 1257 (1978).
[34] R. D. Shannon and C. T. Prewitt, Acta Crystallogr., Sect. B **25**, 925 (1969).
[35] Edward S. Gaffney and Thomas J. Ahrens, J. Geophys. Res. **78**, 5942 (1973).
[36] Surinder M. Sharma and Y. M. Gupta, Appl. Phys. Lett. **54**, 84 (1989).
[37] Serge Desgreniers, Yogesh K. Vohra, and Arthur L. Ruoff, Solid State Commun. **70**, 705 (1989).